LASER & PHOTONICS REVIEWS
www.lpr-journal.org

Integrated Resonant Electro-Optic Comb Enabled by Platform-Agnostic Laser Integration

Isaac Luntadila Lufungula,[#] Amirhassan Shams-Ansari,[#] Dylan Renaud, Camiel Op de Beeck, Stijn Cuyvers, Stijn Poelman, Maximilien Billet, Gunther Roelkens, Marko Lončar, and Bart Kuyken**

The field of integrated photonics has significantly impacted numerous fields including communication, sensing, and quantum physics owing to the efficiency, speed, and compactness of its devices. However, the reliance on off-chip bulk lasers compromises the compact nature of these systems. While silicon photonics and III-V platforms have established integrated laser technologies, emerging demands for ultra-low optical loss, wider bandgaps, and optical nonlinearities necessitate other platforms. Developing integrated lasers on less mature platforms is arduous and costly due to limited throughput or unconventional process requirements. In response, a novel platform-agnostic laser integration technique is proposed, utilizing a singular design and process flow, applicable without modification to a diverse range of platforms. Leveraging a two-step micro-transfer printing method, nearly identical laser performance is achieved across platforms with refractive indices between 1.7 and 2.5. Experimental validation demonstrates strikingly similar laser characteristics between devices processed on lithium niobate and silicon nitride platforms. Furthermore, the integration of a laser with a resonant electro-optic comb generator on the thin-film lithium niobate platform is showcased, producing over 80 comb lines spanning 12 nm. This versatile technique transcends platform-specific limitations, facilitating applications like microwave photonics, handheld spectrometers, and cost-effective Lidar systems, across multiple platforms.

1. Introduction

Integrated photonics has sparked a revolution in various fields, including optical communication,[1,2] quantum systems,[3,4] ranging,[5] sensing,[6] metrology,[7] radio frequency photonics,[8] and intelligent computing.[9] This transformative wave is driven by the capability of integrated photonics to enable high-speed, cost-effective, power-efficient, and compact devices. As a result of this expanding utility and growing demand, there is a conspicuous interest in the integration of lasers into various photonics platforms. This integration facilitates increased complexity, reduces the physical footprint, and ultimately lowers the overall cost of these integrated photonic devices.

Although silicon photonics or III-V platforms like InP have well-developed integrated lasers,[10,11] typically used in telecommunication, other platforms are better suited for applications such as nonlinear photonics, ranging, and spectroscopy. In particular ultra-low optical

I. Luntadila Lufungula, C. Op de Beeck, S. Cuyvers, S. Poelman, M. Billet, G. Roelkens, B. Kuyken
Photonics Research Group
Department of information technology (INTEC)
Ghent University-imec
Ghent 9052, Belgium
E-mail: bart.kuyken@ugent.be

The ORCID identification number(s) for the author(s) of this article can be found under https://doi.org/10.1002/lpor.202400205

[#]Isaac Luntadila Lufungula and Amirhassan Shams-Ansari contributed equally to this work.

DOI: 10.1002/lpor.202400205

I. Luntadila Lufungula, C. Op de Beeck, S. Cuyvers, S. Poelman, M. Billet, G. Roelkens, B. Kuyken
Center for Nano- and Biophotonics (NB-Photonics)
Ghent University-imec
Ghent 9052, Belgium

A. Shams-Ansari, D. Renaud, M. Lončar
John A. Paulson School of Engineering and Applied Sciences
Harvard University
Cambridge, Massachusetts MA 02138, USA
E-mail: loncar@seas.harvard.edu

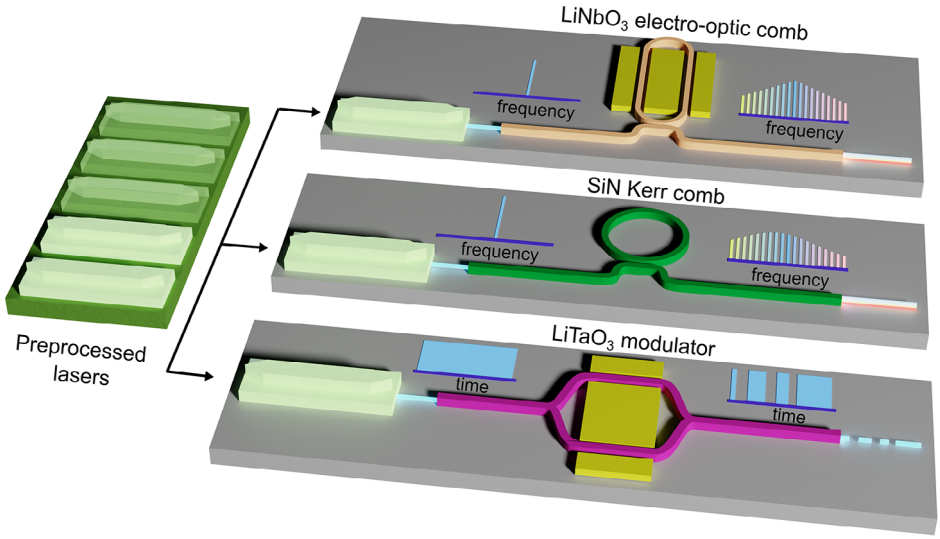

Figure 1. Conceptual representation of platform-agnostic laser integration: The envisioned platform-agnostic laser integration technique utilizes the same design and process flow for a wide range of nanophotonic platforms, eliminating platform-specific design and fabrication. The fabrication of the laser is decoupled from the target platform by prefabricating its gain and cavity sections on separate substrates and transferring them onto the target platform. A platform agnostic design ensures consistent performance across platforms, facilitating the miniaturization of a diverse array of devices available on different platforms. The figure depicts some examples: fully integrated lithium niobate electro-optic combs, silicon nitride Kerr combs, and lithium tantalate modulators.

loss, larger transparency window, larger bandgap, and optical nonlinearities are hard to achieve in the established platforms. If one or more of these characteristics are required, new, often comparatively low index, platforms such as Thin-film Lithium Niobate (TFLN),[12] Thin-film Lithium Tantalate (TFLT),[13] Si_3N_4,[14] and tantalum pentoxide[15] (tantala, Ta_2O_5) can offer a solution. Each of these platforms could cater to a wide range of applications with integrated lasers but the design of scalable laser-integrated photonic devices on these platforms presents considerable challenges.

We note that both hybrid (chip-to-chip) and heterogeneous (on-chip) integration techniques,[16] are costly and challenging. This is mainly due to either low throughput or non-conventional process development, which is imposed by the specific limitations of each platform. For hybrid integration, the fabrication process is simplified by eliminating any co-processing of the laser material and the platform material. Butt coupling is used to couple the light of the laser on one chip to the platform circuit on another chip, enabling pretesting and post-selection of laser dies. However, this die-to-die integration results in low throughput and requires a coupling region tailored to each platform to ensure low-loss coupling and stable laser operation. Conversely, conventional heterogeneous integration techniques, such as wafer bonding or epitaxial growth, offer high throughput by processing the full laser stack in-situ on the platform chip. This, however, requires developing a new process flow compatible with both the gain medium and the platform resulting in a long development time, and a more complex process flow. In other words, conventional hybrid and heterogeneous integration techniques necessitate defining either the cavity or the coupling interface on the platform material leading to significant costs due to the need for platform-specific fabrication processes and designs.

Our goal is to develop a laser integration technique that is platform agnostic; a single design and process flow are used without modification for fabricating scalable integrated lasers across a large variety of platforms (see **Figure 1**). To realize this, we leverage micro-transfer printing, a heterogeneous integration technique allowing the simultaneous transfer of multiple fully processed devices from one chip to another, combining scalability with prefabrication.[17,18] We transfer a full laser in two printing steps and optimize the process to ensure near-identical laser performance on a variety of integrated photonic platforms without the need for additional design optimization or process development.

We first show our technique's compatibility with a wide range of platforms, with refractive indices ranging from 1.7 to 2.5. We then experimentally validate our findings by showing near-identical laser characteristics for identically processed lasers integrated on TFLN and SiN platforms. Additionally, we demonstrate a laser-integrated resonant electro-optic (EO) comb by integrating our laser along with a frequency comb generator on the TFLN platform, resulting in a spectrum spanning 12 nm in the telecommunication region. The latter illustrates our platform-agnostic approach's ability to rapidly develop fully integrated devices on new platforms.

2. Results

2.1. Platform Agnostic Laser Integration Enabled by Micro-Transfer Printing

To guarantee that the laser behaves uniformly across platforms, its manufacturing process should not rely on the specific photonic platform being utilized and a single laser design and geometry should be universally applicable across platforms. Here, we first argue that micro-transfer printing is particularly suited for platform-agnostic fabrication since it enables processing the laser components separately and only then transferring them to

the target platform. We then describe a platform agnostic design realized with a two-step transfer printing process: printing first the laser's cavity followed by its gain section. Finally, we describe how to use this process to fabricate platform-agnostic lasers over a large wavelength range, by combining different gain sections with variations of our optimized cavity.

Micro-transfer printing[19,20] is a novel integration technique that combines the minimal post-processing of hybrid integration with the scalability of heterogeneous integration. Pieces (coupons) of the source material are patterned and underetched, then picked up through adhesion with a Polydimethylsiloxane (PDMS) stamp and finally printed on the target material. Due to the viscoelastic nature of PDMS, its adhesion is sensitive to pressure. Thus, by gradually releasing the stamp after printing, the coupon remains attached to the target. This controllable stamp-coupon adhesion enables printing on any material through Van der Waals forces or a thin adhesion agent like benzocyclobutene (BCB). Importantly, this technique facilitates the simultaneous printing of multiple fully-processed coupons (utilizing arrayed stamps), thereby enabling large scale integration and device post-selection. The possibility of pre-processing complete laser stacks coupled with the non-specificity of the transfer technique makes it an ideal candidate for platform agnostic laser integration.

Previously, however, laser integration with micro-transfer printing required platform-specific considerations. It usually involves printing a III-V amplifier coupon onto a low-loss cavity on the target chip to facilitate lasing. The cavity can be an on-chip filter like an add-drop Vernier combined with a Sagnac reflector,[21] or a quarter-wave shifted distributed feedback (QWSDFB) grating cavity.[22,23] In either case, platform-specific designs for the cavity are required, as the cavity resonance wavelength and shape depend on the platform index (defined as the refractive index of the waveguiding layer), the material stack, and the waveguide propagation losses.

Furthermore, good coupling between the gain material and low index platforms is challenging since even narrow tapers in the usually "thick" (≈ 4 µm), high index (n ≈ 3.5) III-V stack are not sufficient to ensure high-efficiency coupling to low index materials such as LN ($n = 2.2$). This can be addressed with a thin intermediate layer of a higher index material such as Si (n = 3.4) with narrow tapers fabricated using mature processing.[21] Depositing this intermediate layer, however, requires extra in situ processing steps such as deposition and etching that can compromise existing devices on the same chip.

In our approach, we instead print a prefabricated silicon coupon on the platform material that combines the intermediate coupling section with a laser cavity, by including both a linear taper and a QWSDFB grating on the coupon (details in the next section). To finalize the laser we then print a III-V gain coupon on top of the silicon grating creating a Si/III-V DFB laser cavity (see **Figure 2a**).

This allows us to separately pre-process the III-V coupon containing the gain section and the silicon coupon containing both the cavity and the coupling section. It also opens up the possibility of combining a III-V gain section with different silicon cavities with distinct resonance wavelengths, generating a family of platform-agnostic lasers across the whole gain bandwidth. Importantly these silicon coupons with different cavities can be processed on the same source wafer. Furthermore, the wavelength range can be further extended by utilizing multiple III-V coupons, prefabricating them on different chips with distinct material stacks.

To show the potential of this approach we plot the calculated relative lasing powers and lasing wavelengths for different combinations of coupons in Figure 2b (details in the Experimental Section). We combine three existing prefabricated amplifier coupons (details in Section S1, Supporting Information) with optimized silicon coupons (see next section) with a fixed taper and varying QWSDFB pitches, where for each wavelength the matching QWSDFB pitch is assumed (see Figure 2b inset). The figure shows this approach can be used to fabricate efficient lasers for platforms with platform indices between 1.7 and 2.5 and a wide range of lasing wavelengths ($1450 < \lambda < 1600$ nm).

2.2. Optimization of the Coupon Designs

To optimize the platform-agnostic operation of the laser we have to address its three sections: the combined III-V/Si DFB laser cavity, the coupling section from the cavity to the silicon waveguide, and the coupling section from the silicon waveguide to the platform. We will show that the relatively high indices of the Si and III-V enable a platform-agnostic cavity and coupling section to the silicon waveguide by having strong optical confinement in the printed layers instead of the platform material. The silicon taper design will however be crucial to ensure efficient coupling between different platforms and the silicon waveguide. We will also show that the wavelength independence is a serendipitous byproduct of the platform-agnostic optimization.

We optimize the different laser sections using Lumerical Mode and Eigenmode Expansion (EME) simulations with a model material stack for the considered photonic platforms consisting of a 600-nm thick platform material ($n = n_{\text{platform}}$) with partially etched waveguides 300 nm deep on top of 2-µm of buried oxide ($n = 1.55$) with a Si ($n = 3.4$) substrate. We note however that the results obtained in this section are not dependent on the specific stack but are representative for any common material stack as will be shown in the experiments and Section S3 (Supporting Information).

First, we consider the laser cavity, a QWSDFB grating in the silicon with the III-V gain material on top, where the resonant wavelength λ_{DFB} and reflectivity R are determined by:

$$\lambda_{DFB} = 4\Lambda \frac{n_{\text{etched}} n_{\text{unetched}}}{n_{\text{etched}} + n_{\text{unetched}}} \tag{1}$$

$$R = \left[\frac{n_{\text{etched}}^{\frac{2L}{\Lambda}} - n_{\text{unetched}}^{\frac{2L}{\Lambda}}}{n_{\text{etched}}^{\frac{2L}{\Lambda}} + n_{\text{unetched}}^{\frac{2L}{\Lambda}}} \right]^2 \tag{2}$$

There are three critical parameters for the cavity design, the length of the grating (L), the pitch Λ and the effective refractive indices of the etched (n_{etched}) and unetched ($n_{unetched}$) grating sections. These effective refractive indices $n_{\text{unetched}} \approx 3.20$ and $n_{\text{etched}} \approx 3.23$ can be retrieved from mode simulations on different cross-sections (**Figure 3a**) and show little dependence on the platform material since the optical mode is almost completely confined in the Si and III-V. As a consequence, the lasing wavelength for a grating with a specific pitch shifts less than ≈50 pm

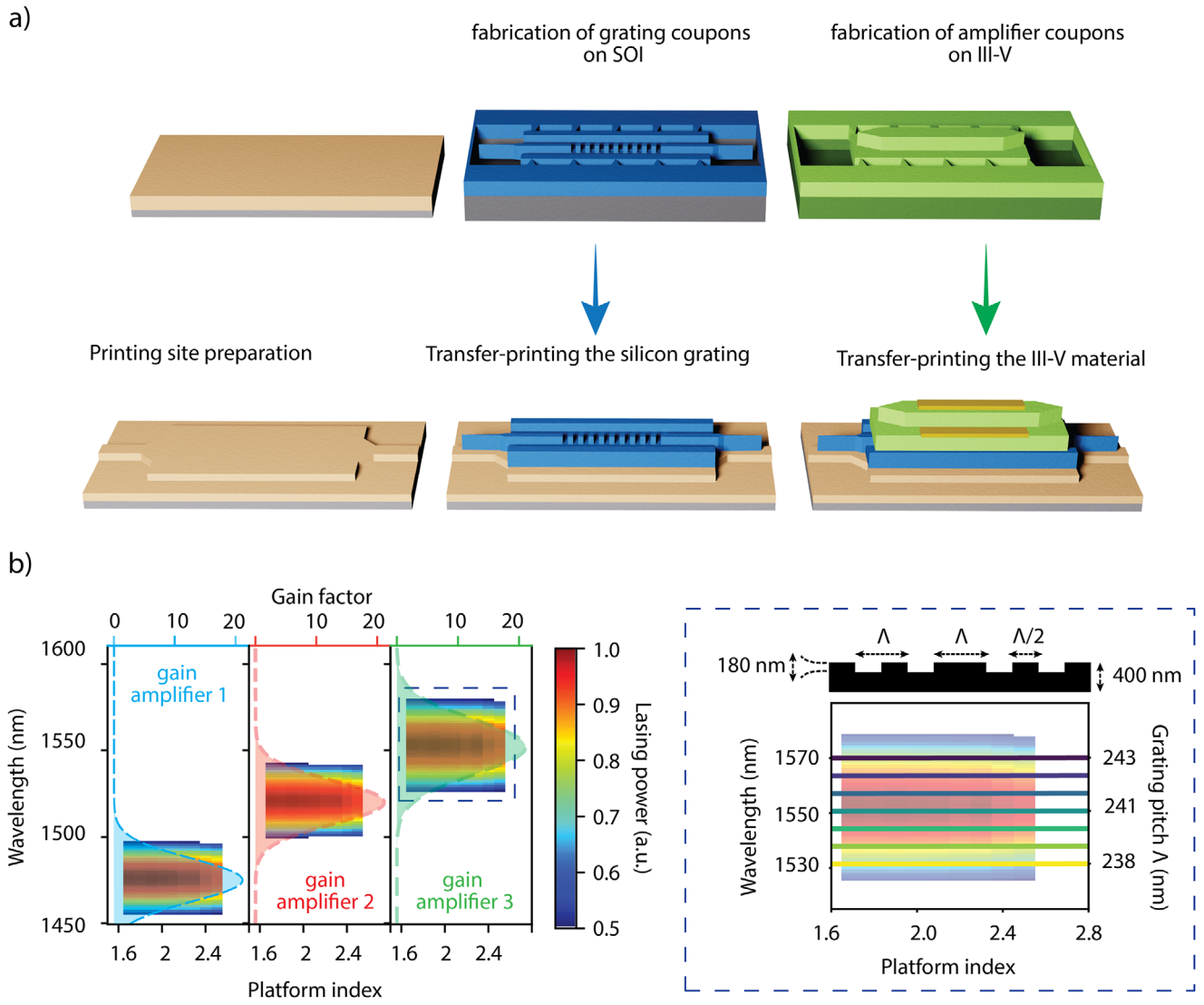

Figure 2. Fabrication process and design space for the platform-agnostic laser integration technique: a) The different fabrication steps of our technique are shown. Left panel: the printing site for the coupons is etched on the target photonics platform. Middle panel: the silicon coupon with a shallow-etched grating cavity and tapers is transferred from a prefabricated silicon-on-insulator wafer and printed onto the printing site. Right panel: a prefabricated III-V coupon with tapers included is then printed on top of the silicon grating serving as the gain section. This step is followed by the fabrication of electrical contacts to realize the final laser. b) The normalized lasing powers of lasers consisting of combinations of different silicon grating coupons and III-V gain coupons calculated for a range of platform indices and lasing wavelengths. Different gain bandwidths are provided by three III-V coupons with distinct stacks while the exact wavelength for each laser is fixed by selecting a silicon coupon with the corresponding grating pitch. Lasers of wavelengths between 1460 and 1580 nm can be fabricated on any platform with an index between 1.7 and 2.5 with the same set of prefabricated coupons. Relative lasing powers lower than 0.5 are not shown. The inset shows the lasing range for amplifier three with the cavity grating pitches and their corresponding lasing wavelengths superposed. A 1 nm shift in the pitch Λ results in a 6.4 nm shift in the lasing wavelength. The wavelengths in between can be addressed by current tuning and thermal tuning. The cavity grating cross-section is shown on top of the inset.

for platforms indices ranging from 1.7 to 2.5 (see Section S4, Supporting Information). By keeping L fixed (450 μm) and varying Λ, platform agnostic lasers at different wavelengths can thus be demonstrated (see Figure 2b inset).

Then we consider the coupling section consisting of two parts, first the light coming out of the laser cavity is coupled from the III-V/Si waveguide into the silicon waveguide after which this light gets coupled to the platform waveguide (see Figure3a). For the first part, the optical mode is still mainly confined in the silicon and the III-V coupons so the coupling is not dependent on the photonics platform and a transmission of 95 % is achieved between the cavity and the silicon waveguide using an adiabatic coupler in the III-V as described in ref. [24].

The second coupler, however, interfaces directly with the target photonics platform. To ensure coupling between a variety of nano-photonic platforms and the silicon coupon, the coupler's dimensions must cover the required effective index matching points for a wide range of platform indices. As we want to keep the printing site geometry of the platform fixed (3μm waveguide at the coupler) this index matching point will correspond to differ-

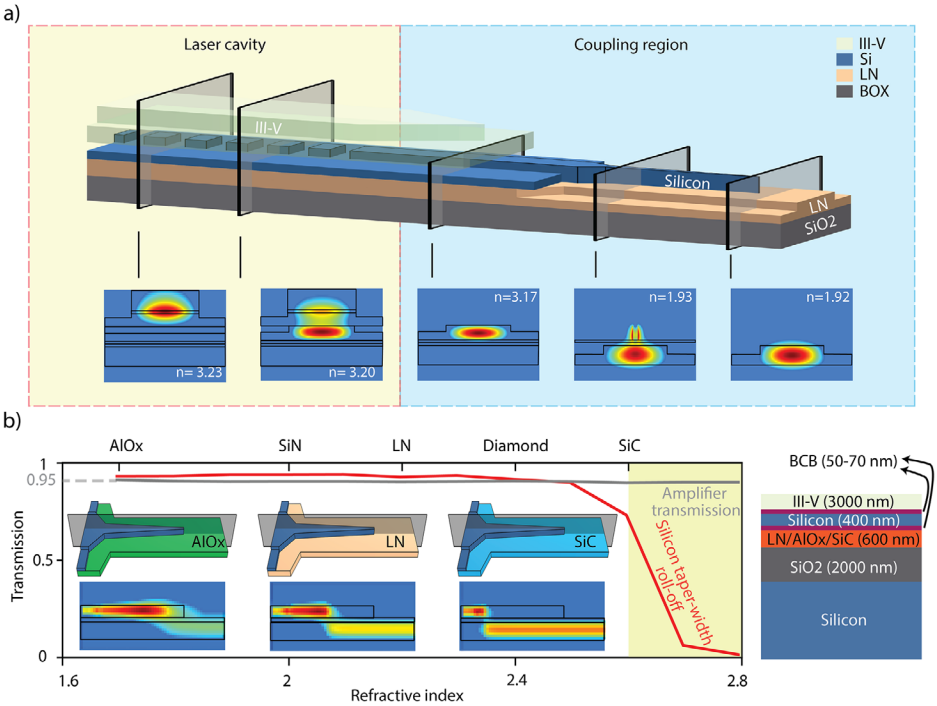

Figure 3. Platform-agnostic heterogeneous laser integration simulation and design: a) 3-D schematic of the different coupling interfaces between the platform material (indexes based on the thin film lithium niobate platform), the silicon coupon, and the amplifier coupon. The cross-sectional electrical field distribution of the TE optical modes at different locations and the associated effective index are shown below. In the laser cavity, the mode is solely confined in the silicon and III-V enabling the platform-agnostic lasing concept. b) Simulated coupling efficiency (transmission) between the silicon coupon and the platform (red line) and the III-V and the silicon coupon (grey line) for various values of refractive indices. The transmission between the III-V and silicon is always 95% since the mode does not interact with the platform material there. The insets are 3-D schematics, and Eigenmode Expansion (EME) simulation results (side-view) for the optical mode coupling between the Si coupon and AlO_x, lithium niobate and SiC waveguides (600 nm thick device layer with a 300 nm slab on top of 2 µm of oxide, 3 µm wide waveguides). They show that the phasematching point shifts to wider points of the taper for higher platform indices. The yellow-shaded region shows a fast roll-off in the platform to Si transmission for indices higher than 2.5 due to the Si taper not being wide enough to match the effective index between the taper and the wider, relatively high index waveguide underneath. The material stacks used in these simulations are shown on the right. Both plots are considered for a wavelength of 1570 nm.

ent widths of the silicon coupler for different platforms. To cover a large range of widths while keeping the coupling adiabatic, we adopt a linear taper geometry for the platform-silicon couplers.

The taper is optimized by using Lumerical Eigenmode Expansion to calculate the transmission and varying both the taper dimensions and the platform index $n_{platform}$ and keeping the wavelength fixed. By comparing these transmissions we can choose an optimal design within the fabrication constraints covering a wide range of indices. The optimized silicon taper has a narrow tip of 120 nm which tapers out to 340 nm width over 200 µm (seeSection S5, Supporting Information) and has a simulated transmission at 1570 nm of > 93% for $n_{platform} = 1.7–2.5$, with a peak transmission of 99.5% for $n_{platform} = 2$ (see Figure 3b). For different material indices the optical mode transfers from the silicon taper to the platform at different spots along the taper, this is where there is a match between their effective refractive indices. When the platform index rises, the transition point moves in the direction of the wider section of the taper. This shift continues until a substantial decline in coupling efficiency is observed for platform indices exceeding 2.5, primarily due to the constrained width (340 nm) of the wider section of the taper (Figure 3b-insets).

The width of the silicon taper is constrained there because it must be significantly smaller than the width of the printing site underneath (3 µm) to avoid a dramatic drop in the coupling efficiency in case of lateral misalignment. For the optimized taper and $n_{platform} = 1.7–2.5$, $\lambda = 1570$ this drop is less than 5% for a lateral offset of 500 nm of the silicon coupon, which is three times the standard deviation ($3\sigma = \pm$ 500 nm) of state of the art transfer printing tools (see Section S6, Supporting Information for the wavelength dependence). For higher index platforms, one could use a wider printing site but this would come at the cost of exciting higher order modes in the waveguide for lower index platforms.

Also a lateral offset of 500 nm for III-V coupon results in less than 2 % drop in transmission across our index range at 1570 nm (see Section S6, Supporting Information for the wavelength dependence).

We additionally note that the transmission of the full coupling section consisting of the silicon and III-V tapers is not significantly affected by the operation wavelength, with $T(\lambda, n_{platform}) >$ 80% for $n_{platform} = 1.7–2.5$ and $\lambda_{laser} = 1460–1580$ nm spanning most of the gain bandwidth of the three amplifiers considered (see Section S3, Supporting Information). This wavelength insensitivity was not specifically optimized for but is a byproduct of the platform agnostic design. While we use a single taper design here, the operating range could further be extended by using multiple designs for different wavelength and index ranges.

2.3. Experimental Demonstration of Platform Agnostic Laser Integration

To experimentally demonstrate the platform-agnostic laser integration technique we fabricate lasers using the same coupons on SiN and LN. We first describe the fabrication of the Si and III-V coupon chips, and then we elaborate on the preparation of the SiN and TFLN platform chips, followed by the printing process. Finally, we discuss the laser measurements on both platforms and show that the laser performance is nearly identical.

For the Si coupons we start from a silicon-on-insulator sample with a 400 nm silicon layer on top of a 2 µm BOX layer. We partially etch (180 nm deep) the silicon waveguides and the QWSDFB grating ($\Lambda = 247$ nm) and define the coupons by fully etching a rectangular trench around the waveguides with grating, while retaining some tethers connecting the coupon to the surrounding silicon (see Experimental Section). The coupons are then underetched, resulting in suspended coupons with partially-etched waveguides and a QWSDFB grating (details in the Experimental Section). The processing of the III-V amplifier coupons is described in ref. [24]. In fact the amplifier coupons we use come from the same chip used in ref. [24], which shows the robustness of these coupons and makes it very simple to integrate them on new platforms as they do not need to be refabricated. The prefabricated silicon and III-V source chips are then ready to be used both containing hundreds of coupons to be printed.

The SiN target chip is fabricated on a 300 nm thick SiN on 3.3 µm of oxide on a silicon substrate with fully-etched waveguides while the TFLN target chip is fabricated on 600 nm of x-cut TFLN with partially etched (300 nm etch depth) waveguides on 2 µm oxide on a silicon substrate[25,26] and an 800-nm thick oxide cladding (details in the Experimental Section).

The printing site for both SiN and TFLN is defined as a single-mode waveguide tapering to a 3 µm wide section, which is 130 µm long after which it tapers to > 60 µm wide section. The 3 µm waveguide part will be where the Si taper couples the light to the platform, while the > 60 µm wide section is where the cavity will be printed (see Figure 2a). For the LN, we then open a window on top of the printing site, etching the cladding down to 100 nm to ensure good coupling efficiency between the coupons and the LN, while the SiN is already uncladded.

After the circuits on the LN and SiN target chips are defined, the fabrication steps are identical. We first spin coat 50–70 nm of Benzocyclobutene (BCB) to provide extra adhesion for the transfer printing process and deposit an Al_2O_3 etch stop layer (35 nm). We then transfer-print identical silicon coupons containing the QWSDFB ($\Lambda = 247$ nm) and an access waveguide on top of the printing site on each platform. Subsequently, the silicon tapers are patterned and fully etched with the Al_2O_3 etch stop layer protecting the underlying platform. This step requires a degree of process compatibility as the patterning of the taper can be subtly influenced by the underlying platform. As part of future improvements, it will be incorporated into the coupon preprocessing, mitigating any platform-specific fabrication considerations.

This is followed by another round of BCB spin coating and printing the same amplifier (amplifier 3) coupons with included tapers on both chips. We then cover everything with 3 µm of BCB, open the vias, pattern the electrodes, and deposit the Ti-Au for the final contacts (details in the Experimental Section). The amplifier coupons printed have gain centered around 1550 nm and the QWSDFB grating ($\Lambda = 247$ nm) in the silicon coupons will select the target wavelength within the gain bandwidth (see Figure 2b inset).

The compound yield of the two printing steps remains high as micro-transfer printing can be a very high yield process. For instance, in ref. [18], a yield of 99.99% was demonstrated after printing thousands of SiN and GaN coupons. For our two-step printing process, all coupons were printed successfully and other studies with Si[27] or III-V coupons[28,29] also show near-perfect success rate. The lack of failures indicates a high yield however, a large number of lasers would need to be printed to accurately estimate the yield.

We use a current source to pump the lasers and measure a threshold current of approximately 75 mA for both devices (see Section S8, Supporting Information). At 130 mA the lasers reach their maximum lasing power as higher drive current will result in lower power due to self-heating effects. At this drive current, the emission spectra of the laser on SiN and LN are near-identical (see **Figure** 4b): single-mode lasing with a lasing wavelength of 1574.6 nm and an on-chip power of −10.5 and −11.5 dBm, respectively. At different drive currents, the lasing powers and wavelengths also remain very similar (see Section S8, Supporting Information).

It is important to note that the Si and III-V coupons printed are identical not only in design but that they come from the same prefabricated chip. This means any systematic errors introduced during fabrication will affect both coupons ensuring identical operation and allowing for pretesting on a test platform e.g., SiN before printing them on a harder-to-fabricate platform like low-loss LN.

Aside from systematic fabrication errors, random local imperfections are minimal for both silicon and III-V due to their process maturity. Moreover, the lasing wavelength can be finely tuned by changing the pump current (see Section S7, Supporting Information), further reducing the impact of random local fabrication errors. Finally we remark that the compared lasers are printed on platforms with different platform indices, as well as different material stacks: 300 nm SiN on 3300 nm SiO_2 on Si and 600 nm LN on 2000 nm SiO_2 on Si,while retaining near-identical laser performance, demonstrating that the process is truly platform agnostic (see also Section S3, Supporting Information).

2.4. Fully Integrated Electro-Optic Frequency Comb

To demonstrate the utility of platform-agnostic laser integration we use the laser on LN to realize a fully integrated electro-optic comb. We first discuss why this is a relevant example, then we detail the co-integration of the laser with the EO comb generator and discuss the characteristics of the resulting comb.

While numerous examples of on-chip photonic advancements can benefit from laser co-integration, we specifically focus on using our technique to integrate a laser with an electro-optic frequency comb generator. Compared to other frequency comb sources, EO combs have several advantages such as fundamental coherence, smaller comb spacing, flexibility in the center operating wavelength, and reconfigurability of the comb spacing.[30]

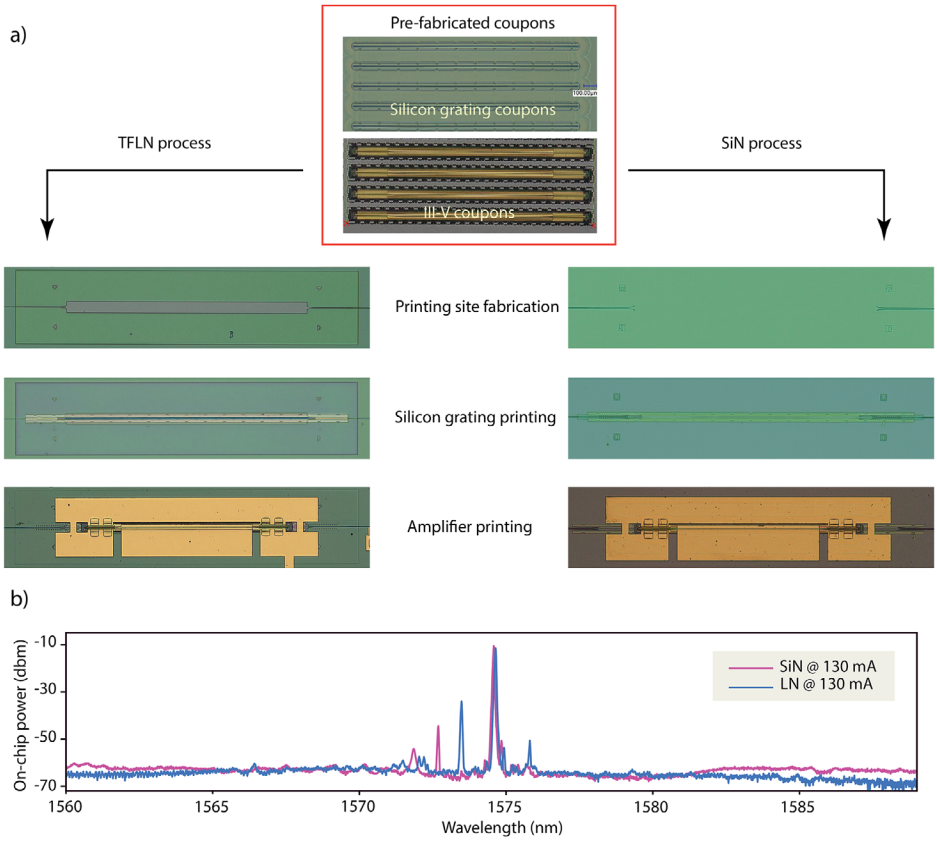

Figure 4. Experimental results for platform-agnostic lasers transfer printed onto thin-film lithium niobate and silicon nitride platforms. a) The silicon cavity coupon, and III-V gain coupons (shown at the top) are transferred to printing sites in TFLN and SiN. The laser fabrication is finalized by patterning the extended electrodes for driving the lasers. b) Laser emission spectrum for both lasers at 130 mA showing a near identical emission wavelength at 1574.6 nm. The limited sideband suppression is due to the minimum resolvable features in the silicon grating.

Despite earlier demonstrations of laser integration with thin-film lithium niobate platforms,[31–33] there is yet to be a demonstration of a fully integrated resonant-based electro-optic comb source.

We realize this device by first fabricating a TFLN circuit consisting of a transfer printing site connected through single-mode waveguides to a high Q racetrack cavity with electrodes along the straight arms (**Figure 5a**) and then printing the laser on the transfer printing site as described above.

An EO comb can then be generated by coupling the laser into the racetrack resonance by tuning its frequency to a resonance frequency f_0. The electro-optic effect of LN is then used to modulate the refractive index of the two arms of the racetrack resonator, resulting in pure phase modulation of the circulating light. By matching the modulation frequency to the ring's free spectral range (FSR) frequency $f_{RF} = f_{FSR}$, two sidebands are generated at $f_0 - f_{FSR}$ and $f_0 + f_{FSR}$ which in turn will be resonant, build up in power, and generate further sidebands, building up a comb with a spacing of f_{FSR}. The efficiency of generating sidebands is proportional to $e^{-\frac{a}{QV}}$,[30] with a the round trip loss, Q the quality factor of the racetrack resonator (here $Q \approx 500k$) and V the RF voltage applied to the resonator arms.[30]

Here, we tune the lasing wavelength into the racetrack resonance at 1574 nm using current tuning (1.5 nm tuning range: see Section S7, Supporting Information) by driving it with 108 mA (2V). At this operation point the integrated laser has -14 dBm of output power and a linewidth of 40 MHz. We then apply EO-modulation at the FSR frequency of 18.9 GHz using an RF source followed by a power amplifier, amplifying the signal to $P_{RF} = 30$ dBm, although most of this power is reflected as the device is not impedance matched. The generated spectrum consists of 80 comb lines with a bandwidth of more than 12 nm and a slope of $-3.5\frac{dB}{nm}$. (see Figure 5c). Although this is a relatively small bandwidth, it could be broadened considerably by incorporating a secondary ring resonator as in ref. [34], increasing the laser power or improving the quality factor of the racetrack resonator. Our integration technique could also be used to combine EO combs centered around different wavelengths on the same chip by using prefabricated silicon coupons with different QWSDFB grating pitches.

The fully integrated comb shown here is a critical step toward the realization of compact frequency-agile spectrometers[35] with high efficiency.[34] It exemplifies the rapid integration that is possible with the platform-agnostic laser integration technique as the lasers can be pretested on a test platform while providing design flexibility and limited in situ tunability of the wavelength.

3. Conclusion

In summary, we have introduced a platform-agnostic technique for rapidly integrating single-mode lasers with center

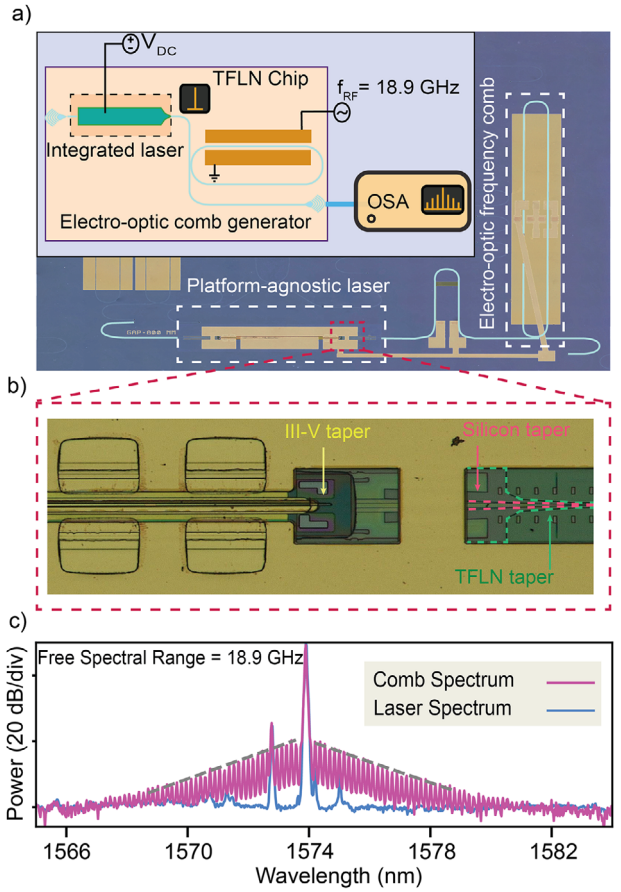

Figure 5. Experimental demonstration of laser-integrated electro-optic frequency comb source. a) Color-corrected micrograph of the fabricated resonant electro-optic frequency comb source integrated with a platform agnostic laser. the inset shows the schematic of the measurement setup. b) Zoom-in image of the coupling region showing all transitions from TFLN to the silicon coupon, and from the silicon to the III-V amplifier coupon. c) Measured output spectrum of the EO comb generated from the microring resonator, demonstrating a bandwidth exceeding 12 nm and more than 80 comb lines with a spacing of 18.9 GHz and a slope of −3.5 $dBnm^{-1}$.

wavelengths between 1460 and 1580 nm onto photonics platforms with refractive indices ranging from 1.7 to 2.5. This technique consists of a two-step transfer printing process, printing first a silicon coupon containing the cavity and the coupling section and then printing a III-V coupon containing the gain section. The design of the coupling section and the strong confinement of the light in the printed layers avoid the need for any platform-specific design or fabrication. This enables off-chip fabrication and pretesting and optimization of the laser on a test platform ensuring predictable and high-yield lasing operation for future platforms. Importantly the silicon and III-V coupons can be prefabricated and remain stable for years, allowing for off-the-shelf processing. Moreover, different cavity and gain coupons can be readily combined allowing for flexibility in lasing wavelength and other laser characteristics. This approach is particularly valuable for prototyping and rapidly integrating lasers on evolving platforms[36,37] and co-integrating lasers of different wavelengths.[38–40]

We have validated our approach by successfully implementing lasers on both SiN and TFLN platforms, achieving nearly identical performance in terms of lasing wavelength and power. Furthermore, we have demonstrated the utility and ease of integration of our technique by showcasing a fully-integrated resonant electro-optic frequency comb on the TFLN platform, generating more than 80 comb lines over 12 nm from the on-chip laser.

Looking ahead, our focus will be on transferring the remaining on-chip post-processing to preprocessing by etching the tapers of the silicon coupon before printing instead of after. This would simplify on-chip processing to just the two transfer printing steps and depositing electrodes, avoiding post-processing of the final device.

To enable the utilization of our technique across a broad spectrum of applications, we will also prioritize enhancing the output power of our lasers. By adopting an asymmetric cavity design, incorporating thermal vias to mitigate self-heating, optimizing the amplifier coupons for high saturation power or printing a booster amplifier to amplify the laser output,[41] higher-power lasers can be facilitated within our platform-agnostic laser scheme.

Aside from optimizing the technique we aim to integrate lasers on various platforms to realize fully integrated devices with different applications. The implementation of our miniaturized, power-efficient integrated lasers with various comb sources would pave the way for compact, high-performance transceivers and microwave photonic systems.[42–45] Similarly, the next generation of compact photonic processors[46–48] such as optical neural networks,[49] can benefit from our platform agnostic approach to integrate a large number of laser sources with different characteristics on the same chip. Finally, further optimization of the III-V gain and silicon cavity coupons would improve the laser linewidth and output power, enabling demanding applications in metrology.

4. Experimental Section

Calculation of Lasing Powers for Different Coupon Combinations: In Figure 2b the relative lasing power coupled to the platform is calculated with:

$$P_{\text{laser}}(\lambda, n_{\text{platform}}) = T(\lambda, n_{\text{platform}}) \times \frac{\alpha_m(\lambda, n_{\text{platform}})}{\alpha_m(\lambda, n_{\text{platform}}) + \alpha_i} \times \frac{h\nu}{q}\left[I - I_{\text{th}}(\lambda, n_{\text{platform}})\right] \quad (3)$$

here $T(\lambda, n_{\text{platform}})$ is the power transmission from the laser to the platform material, largely determined by the taper in the silicon coupons, α_i is the internal cavity loss, $h\nu$ is the photon energy and q is the electron charge. α_m is the distributed mirror loss, defined as $\alpha_m = \frac{1}{L}\ln\frac{1}{R}$ with $R(\lambda, n_{\text{platform}})$ the simulated QWSDFB grating reflection dependent on both the wavelength and platform index and L the cavity length. I is the drive current and I_{th} is the threshold current that can be derived for the different amplifiers from the measured wavelength dependent small signal gain $g(I, \lambda)$ and the QWSDFB reflection $R(\lambda, n_{\text{platform}})$. This formula can be interpreted as the amount of surplus electrons converted to photons above threshold $\frac{h\nu}{q}\frac{\alpha_m}{\alpha_m+\alpha_i}(I - I_{\text{th}})$ multiplied by the fraction that is coupled out of the cavity $\frac{\alpha_m}{\alpha_m+\alpha_i}$ and the coupling from the laser to the platform $T(\lambda, n_{\text{platform}})$. The powers shown are calculated assuming $I = 120mA$ and using: the simulated silicon grating reflection, assuming the correct pitch at each

wavelength, the extrapolated (for amplifiers 1, and 2) and measured (for amplifier 3) gain spectra, and the simulated taper transmission (More details in Section S2, Supporting Information).

Fabrication: The Si coupons started from a silicion-on-insulator sample with a 400 nm silicon layer on top of a 2 µm BOX and a Si substrate. Trenches were partially etched, defined by e-beam lithography with an etch depth of 180 nm to define the silicon waveguides and the QWS-DFB grating (Λ = 247 nm) using a reactive ion etch (RIE) with CF_4, H_2 and SF_6. To define the coupons, the same RIE recipe was used to fully etch a rectangular trench around the waveguides with grating, while retaining some tethers connecting the rectangular coupon to the surrounding silicon. Then this silicon coupon was underetched by etching away the silicon oxide underneath using a vapor HF etch. At this point, the coupons were suspended with on top partially etched waveguides with a QWSDFB grating and this source chip was ready to be used. After the coupons were printed tapers were fully etched using the same RIE recipe.

The processing of the III-V amplifier coupons is described in ref. [24]. In fact, the amplifier coupons used come from the same chip used in ref. [22], which shows the robustness of these coupons and makes it very simple to integrate them on new platforms as they do not need to be refabricated. These prefabricated coupons were then ready to be printed.

The SiN target chip was fabricated on a 300 nm thick LPCVD grown SiN material on 3.3 µm of thermally grown oxide. The fully-etched SiN waveguides were defined using e-beam lithography (positive tone AR-P 6200.13) followed by an RIE with CF_4, and H_2 chemistry.

The TFLN target chip was fabricated on 600 nm of x-cut TFLN on 2 µm of thermally grown oxide on a silicon substrate. The waveguides were patterned using E-beam lithography with a negative tone resist (HSQ) and partially etched (300 nm etch depth) with RIE (Ar+) and were later cladded with 800 nm of Inductively Coupled Plasma Chemical Vapor Deposition (ICPCVD) SiO2, followed by an annealing step to recover damages caused by ion implantation.[25,26] The 300 nm etch depth was chosen to maintain the optical confinement, while providing moderate overlap between the optical and microwave fields. Light was coupled from the laser to the race-track resonators (1.6 µm wide waveguides to reduce losses) using a symmetric coupler in the TFLN to reject higher order modes.

Measurement Conditions: In all experiments the lasers were driven using a Keithley 2400 as the current source. The laser output was measured from one of the grating couplers as light is emitted to both sides, the listed powers were all single-side output. The comb and laser spectra were acquired using an Anritsu MS9740A Optical spectrum analyser. The RF voltage applied to the racetrack resonator in the comb experiment was generated by the Rohde & Schwarz SMR40 Signal Generator. All measurements were done with a temperature controller set to 25 °C.

Supporting Information

Supporting Information is available from the Wiley Online Library or from the author.

Acknowledgements

I.L.L. and A.S.-A. contributed equally to this work. This work was funded by Defense Advanced Research Projects Agency (DARPALUMOS) (HR0011-20-C-0137), Air Force Office of Scientific Research (AFOSR) (FA9550-19-1-0376), Fonds Wetenschappelijk Onderzoek (FWO) and Fonds de la Recherche Scientifique (FNRS) under the Excellence of Science (EOS) program (40007560), the European Research Council (ERC) HORIZON Proof of Concept Grant (101069447)and the ERC starting grant ELECTRIC (759483). LN device fabrication was performed at the Center for Nanoscale Systems (CNS), a member of the National Nanotechnology Coordinated Infrastructure Network (NNCI), which was supported by the National Science Foundation under NSF Grant no. 1541959.

Conflict of Interest

M.L. is involved, as a co-founder and board member of HyperLight Corporation, in developing lithium niobate technologies. The remaining authors declare no conflict of interest.

Data Availability Statement

The data that support the findings of this study are available from the corresponding author upon reasonable request.

Keywords

frequency comb, heterogeneous integration, integrated photonics, laser integration, lithium niobate, silicon nitride, transfer printing

Received: February 8, 2024
Revised: April 30, 2024
Published online: July 4, 2024

[1] M. Zhang, C. Wang, P. Kharel, D. Zhu, M. Lončar, *Optica* **2021**, *8*, 652.
[2] A. H. Atabaki, S. Moazeni, F. Pavanello, H. Gevorgyan, J. Notaros, L. Alloatti, M. T. Wade, C. Sun, S. A. Kruger, H. Meng, K. Al Qubaisi, I. Wang, B. Zhang, A. Khilo, C. V. Baiocco, M. A. Popović, V. M. Stojanović, R. J. Ram, *Nature* **2018**, *556*, 349.
[3] E. Pelucchi, G. Fagas, I. Aharonovich, D. Englund, E. Figueroa, Q. Gong, H. Hannes, J. Liu, C.-Y. Lu, N. Matsuda, J.-W. Pan, F. Schreck, F. Sciarrino, C. Silberhorn, J. Wang, K. D. Jöns, *Nat. Rev. Phys.* **2022**, *4*, 194.
[4] G. Moody, V. J. Sorger, D. J. Blumenthal, P. W. Juodawlkis, W. Loh, C. Sorace-Agaskar, A. E. Jones, K. C. Balram, J. C. Matthews, A. Laing, et al., *J. Phys.: Photon.* **2022**, *4*, 012501.
[5] J. K. Doylend, S. Gupta, *Silicon Photon. XV* **2020**, *11285*, 109.
[6] Y. Chen, H. Lin, J. Hu, M. Li, *ACS Nano* **2014**, *8*, 6955.
[7] T. J. Kippenberg, A. L. Gaeta, M. Lipson, M. L. Gorodetsky, *Science* **2018**, *361*, 6402.
[8] D. Marpaung, J. Yao, J. Capmany, *Nat. Photonics* **2019**, *13*, 80.
[9] D. Pérez, I. Gasulla, P. D. Mahapatra, J. Capmany, *Adv. Opt. Photon.* **2020**, *12*, 709.
[10] S. Y. Siew, B. Li, F. Gao, H. Y. Zheng, W. Zhang, P. Guo, S. W. Xie, A. Song, B. Dong, L. W. Luo, C. Li, X. Luo, G.-Q. Lo, *J. Lightwave Technol.* **2021**, *39*, 4374.
[11] X. Duan, Y. Huang, Y. Cui, J. Wang, C. M. Lieber, *nature* **2001**, *409*, 66.
[12] D. Zhu, L. Shao, M. Yu, R. Cheng, B. Desiatov, C. Xin, Y. Hu, J. Holzgrafe, S. Ghosh, A. Shams-Ansari, E. Puma, N. Sinclair, C. Reimer, M. Zhang, M. Lončar, *Adv. Opt. Photonics* **2021**, *13*, 242.
[13] C. Wang, Z. Li, J. Riemensberger, G. Lihachev, M. Churaev, W. Kao, X. Ji, T. Blesin, A. Davydova, Y. Chen, X. Wang, K. Huang, X. Ou, T. J. Kippenberg, *(Preprint) arXiv:2306.16492, v2, submitted: July* **2023**.
[14] D. J. Blumenthal, R. Heideman, D. Geuzebroek, A. Leinse, C. Roeloffzen, *Proc. IEEE* **2018**, *106*, 2209.
[15] L. Splitthoff, M. A. Wolff, T. Grottke, C. Schuck, *Opt. Express* **2020**, *28*, 11921.
[16] P. Kaur, A. Boes, G. Ren, T. G. Nguyen, G. Roelkens, A. Mitchell, *APL Photonics* **2021**, *6*, 6.
[17] E. Margariti, G. Quinn, D. Jevtics, B. Guilhabert, M. D. Dawson, M. J. Strain, *Opt. Mater. Express* **2023**, *13*, 2236.
[18] D. Gomez, K. Ghosal, T. Moore, M. A. Meitl, S. Bonafede, C. Prevatte, E. Radauscher, A. J. Trindade, C. A. Bower, in,*2017 IEEE 67th Electronic Components and Technology Conference (ECTC)*, IEEE, Piscataway **2017**, pp. 1779–1785.

[19] J. McPhillimy, B. Guilhabert, C. Klitis, M. D. Dawson, M. Sorel, M. J. Strain, *Opt. Express* **2018**, *26*, 16679.
[20] G. Roelkens, J. Zhang, L. Bogaert, M. Billet, D. Wang, B. Pan, C. J. Kruckel, E. Soltanian, D. Maes, T. Vanackere, T. Vandekerckhove, S. Cuyvers, J. De Witte, I. L. Lufungula, X. Guo, H. Li, S. Qin, G. Muliuk, S. Uvin, B. Haq, C. Op de Beeck, J. Goyvaerts, G. Lepage, P. Verheyen, J. Van Campenhout, G. Morthier, B. Kuyken, D. Van Thourhout, R. Baets, *IEEE Journal of Selected Topics in Quantum Electronics* **2023**, *29*, 3.
[21] C. O. de Beeck, F. M. Mayor, S. Cuyvers, S. Poelman, J. F. Herrmann, O. Atalar, T. P. McKenna, B. Haq, W. Jiang, J. D. Witmer, G. Roelkens, A. H. Safavi-Naeini, R. Van Laer, B. Kuyken, *Optica* **2021**, *8*, 1288.
[22] B. Haq, J. R. Vaskasi, J. Zhang, A. Gocalinska, E. Pelucchi, B. Corbett, G. Roelkens, *Opt. Express* **2020**, *28*, 32793.
[23] J. Zhang, B. Haq, J. O'Callaghan, A. Gocalinska, E. Pelucchi, A. J. Trindade, B. Corbett, G. Morthier, G. Roelkens, *Opt. Express* **2018**, *26*, 8821.
[24] B. Haq, S. Kumari, K. Van Gasse, J. Zhang, A. Gocalinska, E. Pelucchi, B. Corbett, G. Roelkens, *Laser Photonics Rev.* **2020**, *14*, 1900364.
[25] M. Zhang, C. Wang, R. Cheng, A. Shams-Ansari, M. Lončar, *Optica* **2017**, *4*, 1536.
[26] A. Shams-Ansari, G. Huang, L. He, Z. Li, J. Holzgrafe, M. Jankowski, M. Churaev, P. Kharel, R. Cheng, D. Zhu, N. Sinclair, B. Desiatov, M. Zhang, T. J. Kippenberg, M. Loncar, Reduced material loss in thin-film lithium niobate waveguides, **2022**, (Preprint) arXiv:2203.17133, v1, submitted: Mar 2022.
[27] S. Cuyvers, B. Haq, C. Op de Beeck, S. Poelman, A. Hermans, Z. Wang, A. Gocalinska, E. Pelucchi, B. Corbett, G. Roelkens, K. Van Gasse, B. Kuyken, *Laser Photonics Rev.* **2021**, *15*, 2000485.
[28] J. Zhang, G. Muliuk, J. Juvert, S. Kumari, J. Goyvaerts, B. Haq, C. Op de Beeck, B. Kuyken, G. Morthier, D. Van Thourhout, R. Baets, G. Lepage, P. Verheyen, J. Van Campenhout, A. Gocalinska, J. O'Callaghan, E. Pelucchi, K. Thomas, B. Corbett, A. J. Trindade, G. Roelkens, *APL Photonics* **2019**, *4*, 11.
[29] C. O. de Beeck, B. Haq, L. Elsinger, A. Gocalinska, E. Pelucchi, B. Corbett, G. Roelkens, B. Kuyken, *Optica* **2020**, *7*, 386.
[30] M. Zhang, B. Buscaino, C. Wang, A. Shams-Ansari, C. Reimer, R. Zhu, J. M. Kahn, M. Lončar, *Nature* **2019**, *568*, 373.
[31] A. Shams-Ansari, D. Renaud, R. Cheng, L. Shao, L. He, D. Zhu, M. Yu, H. R. Grant, L. Johansson, M. Zhang, M. Lončar, *Optica* **2022**, *9*, 408.
[32] C. O. de Beeck, F. M. Mayor, S. Cuyvers, S. Poelman, J. F. Herrmann, O. Atalar, T. P. McKenna, B. Haq, W. Jiang, J. D. Witmer, G. Roelkens, A. H. Safavi-Naeini, R. V. Laer, B. Kuyken, *Optica* **2021**, *8*, 1288.
[33] X. Zhang, X. Liu, L. Liu, Y. Han, H. Tan, L. Liu, Z. Lin, S. Yu, R. Wang, X. Cai, *Appl. Phys. Lett.* **2023**, *122*, 8.
[34] Y. Hu, M. Yu, B. Buscaino, N. Sinclair, D. Zhu, R. Cheng, A. Shams-Ansari, L. Shao, M. Zhang, J. M. Kahn, M. Lončar, *Nat. Photonics* **2022**, *16*, 679.
[35] A. Shams-Ansari, M. Yu, Z. Chen, C. Reimer, M. Zhang, N. Picqué, M. Lončar, *Commun. Phys.* **2022**, *5*, 88.
[36] A. E. Dorche, N. Nader, E. J. Stanton, S. W. Nam, R. P. Mirin, in *CLEO 2023*, Optica Publishing Group, Washington, D.C **2023**, p. SM2J.5.
[37] T.-J. Lu, M. Fanto, H. Choi, P. Thomas, J. Steidle, S. Mouradian, W. Kong, D. Zhu, H. Moon, K. Berggren, J. Kim, M. Soltani, S. Preble, D. Englund, *Opt. Express* **2018**, *26*, 11147.
[38] N. Chauhan, A. Isichenko, K. Liu, J. Wang, Q. Zhao, R. O. Behunin, P. T. Rakich, A. M. Jayich, C. Fertig, C. Hoyt, D. J. Blumenthal, *Nat. Commun.* **2021**, *12*, 4685.
[39] K.-J. Boller, *Optics letters* **2021**, *46*, 4904.
[40] M. A. Tran, C. Zhang, T. J. Morin, L. Chang, S. Barik, Z. Yuan, W. Lee, G. Kim, A. Malik, Z. Zhang, J. Guo, H. Wang, B. Shen, L. Wu, K. Vahala, J. E. Bowers, H. Park, T. Komljenovic, *Nature* **2022**, *610*, 54.
[41] J. Zhang, L. Bogaert, B. Haq, R. Wang, B. Matuskova, J. Rimböck, S. Ertl, A. Gocalinska, E. Pelucchi, B. Corbett, J. Van Campenhout, G. Lepage, P. Verheyen, G. Morthier, G. Roelkens, *IEEE Photonics Technol. Lett.* **2023**, *35*, 593.
[42] P. Marin-Palomo, J. N. Kemal, M. Karpov, A. Kordts, J. Pfeifle, M. H. Pfeiffer, P. Trocha, S. Wolf, V. Brasch, M. H. Anderson, R. Rosenberger, K. Vijayan, W. Freude, T. J. Kippenberg, C. Koos, *Nature* **2017**, *546*, 274.
[43] B. Corcoran, M. Tan, X. Xu, A. Boes, J. Wu, T. G. Nguyen, S. T. Chu, B. E. Little, R. Morandotti, A. Mitchell, D. J. Moss, *Nat. Commun.* **2020**, *11*, 2568.
[44] H. Hu, F. Da Ros, M. Pu, F. Ye, K. Ingerslev, E. Porto da Silva, M. Nooruzzaman, Y. Amma, Y. Sasaki, T. Mizuno, Y. Miyamoto, L. Ottaviano, E. Semenova, P. Guan, D. Zibar, M. Galili, K. Yvind, T. Morioka, L. K. Oxenløwe, *Nat. Photonics* **2018**, *12*, 469.
[45] D. T. Spencer, T. Drake, T. C. Briles, J. Stone, L. C. Sinclair, C. Fredrick, Q. Li, D. Westly, B. R. Ilic, A. Bluestone, N. Volet, T. Komljenovic, L. Chang, S. H. Lee, D. Yoon Oh, M.-G. Suh, K. Y. Yang, M. H. P. Pfeiffer, T. J. Kippenberg, E. Norberg, L. Theogarajan, K. Vahala, N. R. Newbury, K. Srinivasan, S. B. Papp, *Nature* **2018**, *557*, 81.
[46] T. Zhou, X. Lin, J. Wu, Y. Chen, H. Xie, Y. Li, J. Fan, H. Wu, L. Fang, Q. Dai, *Nat. Photonics* **2021**, *15*, 367.
[47] B. Bai, Q. Yang, H. Shu, L. Chang, F. Yang, B. Shen, Z. Tao, J. Wang, S. Xu, W. Xie, , W. Zou, W. Hu, J. E. Bowers, X. Wang, *Nat. Commun.* **2023**, *14*, 66.
[48] Y. Bai, X. Xu, M. Tan, Y. Sun, Y. Li, J. Wu, R. Morandotti, A. Mitchell, K. Xu, D. J. Moss, *Nanophotonics* **2023**, *12*, 795.
[49] Y. Shen, N. C. Harris, S. Skirlo, M. Prabhu, T. Baehr-Jones, M. Hochberg, X. Sun, S. Zhao, H. Larochelle, D. Englund, Marin Soljacic, *Nat. Photonics* **2017**, *11*, 441.